Subscale modeling of material flow in orthogonal metal cutting

International Journal of Material Forming (2025) 18:12
https://doi.org/10.1007/s12289-025-01875-x

ORIGINAL RESEARCH

Subscale modeling of material flow in orthogonal metal cutting

Ahmet Semih Erturk[1] · **Ragnar Larsson**[1]

Received: 10 October 2024 / Accepted: 6 January 2025

Abstract
Enhanced simulation capability for the cutting process is crucial to making quick evaluations of cutting forces and temperatures, which are significant for assessing the machinability of the workpiece material and predicting tool wear. In this paper, the material flow in orthogonal cutting, including primary and secondary shear zones, is represented by a viscous/viscoplastic model that includes the temperature-sensitive Johnson-Cook flow stress model. A stabilized staggered finite element procedure is developed to handle incompressible Navier-Stokes material flow in combination with convection-dominated hardening and thermomechanical interaction. To handle material flow at tool-workpiece contact, a mixed method is used to reduce spurious oscillations in contact stresses along with simplified heat transfer in the tool-workpiece interface. A novel feature is that the velocity field is resolved as a subscale field to the velocity field of the distributed primary zone deformation model. It appears that the finite element solution to the subscale material flow model is significantly more cost-effective in contrast to directly addressing the velocity field and compared to the chip-forming simulations (DEFORM 2D). The cutting forces, temperature, and stress-strain state of the material in the critical deformation regions can be accurately estimated using the subscale model. The results obtained show that the trend of the estimated forces and temperatures is consistent with our experimental measurements, the DEFORM 2D simulations, and the experimental data from the literature.

Keywords Finite element method · Johnson-Cook · Material flow · Navier-Stokes · Orthogonal metal cutting

Introduction

In metal cutting processes, short tool life and long machining cycles are key challenges in increasing the quality of components and reducing production costs. This problem becomes particularly important when new material grades are introduced to meet design goals, which require the determination of suitable process parameters. To determine the parameters that require the evaluation of the cutting forces, the temperature, and the tool wear, it is well established to use finite element (FE) simulations of the machining process [1–4]. However, due to the high computational cost of finite element simulations in machining, it is a major incentive to improve modeling and simulation capabilities to make faster assessments of the machinability of the workpiece, by evaluation of the forces and temperature, and also for the inverse identification of the material model parameters.

Various representations of the workpiece material have been used to model the cutting process, such as the Eulerian, Lagrangian, arbitrary Lagrangian-Eulerian (ALE), and particle method (PFEM). In the Eulerian formulation, the material moves through a fixed mesh in a predefined space, whereas in the Lagrangian and ALE formulations, the mesh and the material move together with a reference configuration. The PFEM representation considers the workpiece material as the motion of discrete particles in a Eulerian region governed by the conservation of momentum, mass, and energy. The Eulerian formulation is suitable for cutting simulations for a fixed cutting process region, known before cutting simulation [5], while the Lagrangian formulation is suitable for detailed simulation of chip formation in the cutting process [6]. When forces are evaluated in PFEM, the particles move independently of the mesh combined with continuous mesh updates [7, 8]. However, Lagrangian/ALE/PFEM formulations generally suffer from convergence problems and inaccuracy as a result of distorted elements [9]. The ALE formulation [9] partially eliminates the creation of highly distorted elements and

✉ Ahmet Semih Erturk
erturk@chalmers.se

Ragnar Larsson
ragnar.larsson@chalmers.se

[1] Department of Industrial and Materials Science, Chalmers University of Technology, Göteborg SE-412 96, Sweden

Published online: 13 January 2025

reduces the computational time. However, highly distorted elements can still be formed [10]. To address these issues, remeshing and element deletion approaches are implemented [11–13] to eliminate negative Jacobians present during large deformations. Although these approaches solve some of the issues with the Lagrangian formulation, they also increase computational time.

Since the dominant deformation during metal cutting occurs in the primary and secondary shear zones, we focus in this article on the material flow resolved only in these zones treated as a fixed Eulerian region. Material flow is considered pseudoplastic based on the Navier-Stokes equations (NS) in combination with a semi-analytical model for material flow in the primary shear zone (PSZ) [14, 15]. To obtain a pure Computational Fluid Dynamics (CFD) approach that avoids elasticity, we propose here to adopt a pseudoplastic approach based on a Newtonian viscous/non-Newtonian thermo-viscoplastic flow model, where the viscoplastic part of the material is represented by the Johnson-Cook model (JC) [16]. In addition, a unique mixed method is developed for frictional contact of material flow at the tool-workpiece interface. The method reduces spurious oscillations in contact stresses associated with the conventional regularized frictional/contact formulation [17]. In the literature, examples of the CFD approach can be found for slow processes such as polymers, fresh concrete, sludge, mudflows, food pastes [18, 19], and in some cases also for the silo flow of granular material subjected to large deformations and high strain rates [20]. Furthermore, pseudoplastic behavior can be observed in metal injection molding [21]. In this context, fluid mechanics-based approaches to analyze the machining process at high speeds often assume analytical potential flow modeling for the behavior of the material around the tooltip [22, 23]. Similarly, the temperature distribution in the cutting zone has been addressed using potential theory [24, 25]. However, pure CFD approaches are rarely used for machining simulations.

To further reduce computational cost, the total velocity in this article is subdivided into a subscale velocity field and a smooth long-range velocity field [26]. Long-range fluctuation is synthesized based on the velocity and strain-rate distribution in the PSZ of a semi-analytical model, whereas the subscale velocity is calculated according to the NS equations. The semi-analytical model, called the distributed primary zone deformation (DPZD) model [14, 15], combines machining experiments with the assumed shear zone kinematics in PSZ. Moreover, to address the coupling between the material velocity field and the material evolution of the coupled hardening and temperature, a stabilized staggered FE solution procedure is developed. The results obtained from the presented subscale model in terms of forces, stresses, and temperatures are validated with orthogonal cutting experiments. To evaluate the performance and time efficiency of the subscale model, the results are compared with DEFORM 2D forming simulations and data from the literature.

Subscale material flow model

In this section, the subscale material flow model is established, which consists of the assumed shear rate distribution based on the geometric characteristics of the primary shear zone and the stabilized incompressible NS flow to describe the fine-grained velocity field in the shear zones. The viscous material rheology of the material model is formulated. For the involved material hardening and temperature evolution, separate stabilized weak forms are established to handle the convection-dominated evolution of material hardening and temperature. Concerning the contact boundary, the mechanical and thermal response is formulated at the tool-workpiece contact interface.

Coarse-grained shear rate distribution

The Eulerian region Ω occupies the most important part of the material flow for cutting, as shown in Fig. 1. This region consists of the primary shear zone Ω_{PSZ} and the secondary shear zone Ω_{SSZ}, with stagnant shear flow. To facilitate a cost-effective model for the severe shear flow region Ω_{PSZ}, an assumed coarse-grained shear rate distribution $\bar{\boldsymbol{v}}[\boldsymbol{x}] \in \Omega_{PSZ}$ based on the DPZD model is incorporated [14, 15]. The total velocity of the material thus consists of the course-grained (DPZD governed) part $\bar{\boldsymbol{v}}$ and a subscale velocity field $\boldsymbol{v}^s$ defined as

$$\boldsymbol{v} = \bar{\boldsymbol{v}} + \boldsymbol{v}^s \Rightarrow \boldsymbol{l} = \frac{\partial \boldsymbol{v}}{\partial \boldsymbol{x}} = \bar{\boldsymbol{l}} + \boldsymbol{l}^s \tag{1}$$

where $\boldsymbol{l}$ is the spatial velocity gradient field with a subdivision analogous to the velocity field.

As to the coarse-grained field $\bar{\boldsymbol{v}}$, it is expressed in terms of the normal and tangential basis vectors $\boldsymbol{n}$ and $\boldsymbol{t}$ in Fig. 1b as

$$\bar{\boldsymbol{v}} = v_n \boldsymbol{n} + v_t[s]\boldsymbol{t} \Rightarrow \bar{\boldsymbol{l}} = \dot{\gamma}\, \boldsymbol{t} \otimes \boldsymbol{n} \text{ with } \dot{\gamma} = v_t'[s] \tag{2}$$

where v_t and v_n are the shear and normal velocities related to the DPZD-approximation [15]. It is assumed that the shear strain rate $\dot{\gamma}$ varies in the normal direction, with the coordinate s as shown in Fig. 1, and that $\dot{\gamma}[s]$ has the distribution defined as

$$\dot{\gamma} = \dot{\bar{\gamma}}\, f[s]\,,\; f[s] = \begin{cases} \left(1 + 2\frac{s}{b}\right)^r & -\frac{b}{2} \le s \le 0 \\ \left(1 - 2\frac{s}{b}\right)^r & 0 \le s \le \frac{b}{2} \end{cases} \tag{3}$$

Here, $\dot{\bar{\gamma}}$ is the shear rate of the shear line AB, $f[s]$ is the distribution function in terms of the primary shear zone thickness

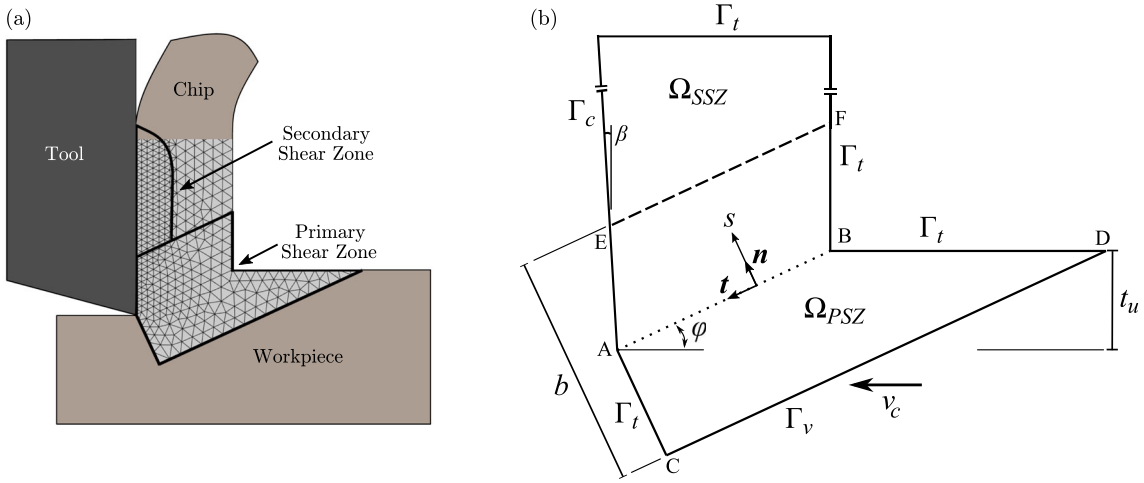

Fig. 1 (a) Modeled region in 2D orthogonal metal cutting that includes primary and secondary shear zones with workpiece material that enters with the cutting speed v_c. (b) Boundaries of the modeled region and detailed primary shear zone, where φ is the shear angle, b is the thickness of the primary shear zone, and t_u is the thickness of the uncut chip (feed). The rake angle is $\beta = 0$ in this study and the dotted line $\in \Omega_{PSZ}$ is the shear line

b and the exponent r. In order to calculate the shear velocity $v_t[s]$, the shear strain rate in Eq. 3 is integrated for both sides of the PSZ as

$$v_t[s] = \begin{cases} v_{t_{CD}} + \dot{\bar{\gamma}} \int_{-\frac{b}{2}}^{s} f[s]ds & -\frac{b}{2} \le s \le 0 \\ v_{t_{EF}} + \dot{\bar{\gamma}} \int_{0}^{s} f[s]ds & 0 \le s \le \frac{b}{2} \end{cases} \tag{4}$$

where $v_{t_{CD}}$ and $v_{t_{EF}}$ are the shear velocities on the borders CD and EF in Fig. 1. Following [14, 15], the corresponding shear and normal velocities can be calculated using the shear angle φ, the rake angle β and the cutting speed v_c as

$$v_{n_{CD}} = v_c \sin[\varphi] = v_{n_{EF}} \tag{5a}$$

$$v_{t_{CD}} = v_c \cos[\varphi], \quad v_{t_{EF}} = -v_c \sin[\varphi] \tan[\varphi - \beta] \tag{5b}$$

Finally, the shear rate $\dot{\bar{\gamma}}$ of the shear line is obtained from the distribution $f[s]$ and the continuity of v_t in $s = 0$. Upon combining Eqs. 3, 4 and 5 we obtain

$$\dot{\bar{\gamma}} = -\frac{1+r}{b} \frac{v_c \cos[\beta]}{\cos[\varphi - \beta]} \tag{6a}$$

$$v_t[s] = v_c \left(\cos[\varphi] - \frac{1}{2} \frac{\cos[\beta]}{\cos[\varphi - \beta]} g[s] \right) \tag{6b}$$

$$v_n = v_c \sin[\varphi] \tag{6c}$$

where the function $g[s]$ is the desired (integrated) distribution of the shear velocity

$$g[s] = \begin{cases} \left(1 + \frac{2s}{b}\right)^{r+1} & -\frac{b}{2} \le s \le 0 \\ 2 - \left(1 - \frac{2s}{b}\right)^{r+1} & 0 \le s \le \frac{b}{2} \end{cases} \tag{7}$$

The distribution functions $f[s]$ and $g[s]$ are visualized in Fig. 2.

Furthermore, the primary shear zone thickness b and the shear angle φ in Eqs. 3 and 5 are determined using [14] as

$$\varphi = \tan^{-1}\left(\frac{t_u}{t_c} \frac{\cos\beta}{1 - (t_u/t_c)\sin\beta} \right) \tag{8a}$$

$$b = \frac{(\tau_0 - \tau_{AB})(\cos\varphi + \sin\varphi) t_u^2 w}{(F_c - F_t)\sin^2\varphi (1 + 2(\pi/4 - \varphi))} \tag{8b}$$

where τ_0 is the shear strength of the material and τ_{AB} is the shear stress at the shear line defined as

$$\tau_{AB} = \frac{(-F_c \cos\varphi + F_t \sin\varphi)\sin\varphi}{t_u w} \tag{9}$$

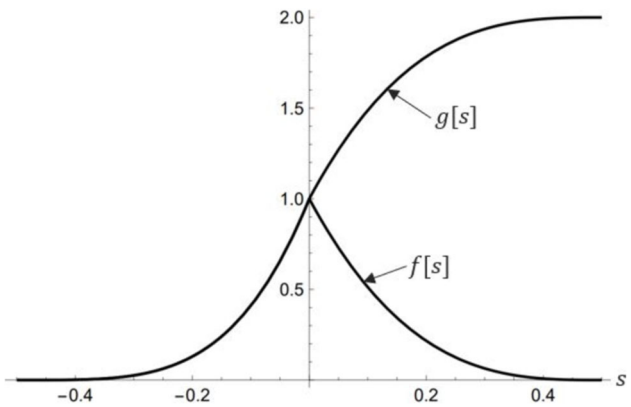

Fig. 2 The distribution functions $f[s]$ and $g[s]$ (when $r = 4$) of the DPZD assumption for the shear strain rate and the consequent shear velocity in the PSZ

It is important to note that the geometry of Ω_{PSZ} is based on the cutting parameters and measurements of the cutting force F_c, the thrust force F_t, and the chip thickness t_c. The cutting parameters involved are the feed t_u, the rake angle β, and the width of the cut w.

Incompressible Navier-Stokes material flow

The principle of mass conservation for the incompressible material with density $\rho[\boldsymbol{x}, t]$ states that

$$\underbrace{\dot{\rho}}_{=0} + \rho \nabla \cdot \boldsymbol{v} = 0 \Rightarrow \rho \nabla \cdot \boldsymbol{v} = 0 \; \forall \boldsymbol{x} \in \Omega \tag{10}$$

The total Cauchy (flow) stress $\boldsymbol{\sigma}$ is formulated in terms of the deviatoric and hydrostatic stresses as

$$\boldsymbol{\sigma} = \boldsymbol{\sigma}_d - p\mathbf{1} \tag{11}$$

where $\boldsymbol{\sigma}_d$ is the stress deviator and p is the pressure associated with the volumetric deformation constraint $\nabla \cdot \boldsymbol{v} = 0$ due to mass conservation. Neglecting the body forces, the strong form of the momentum balance reads

$$\boldsymbol{\sigma}_d \cdot \nabla - \nabla p - \rho \dot{\boldsymbol{v}} = \mathbf{0} \; \forall \boldsymbol{x} \in \Omega \tag{12}$$

where the inertia term includes the material time derivative of the velocity

$$\dot{\boldsymbol{v}} = \boldsymbol{v}_{,t} + \boldsymbol{l} \cdot \boldsymbol{v} \text{ with } \boldsymbol{v}_{,t} := \frac{\partial \boldsymbol{v}}{\partial t} \tag{13}$$

It is clear that the relations (10) and (12) represent the strong form of the incompressible NS equations for the flow of the workpiece material during cutting. In the present context, contact tractions along the contact boundary Γ_c are considered in a weak form to incorporate contact conditions of the material flow. The corresponding weak forms of momentum and mass conservation are formulated by introducing the set $V \times P \times Q$ of kinematically admissible velocities, pressures, and boundary tractions with sufficient regularity. This may be formulated as: find $\{\boldsymbol{v}^s, p, \tilde{\boldsymbol{v}} \in V \times P \times Q\}$ so that for all $\boldsymbol{w}, q, \delta\tilde{\boldsymbol{v}} \in V \times P \times Q$ the following stabilized NS-equations are satisfied

$$\begin{aligned} &\left(\boldsymbol{w}, \boldsymbol{v}_{,t}\right) + c(\boldsymbol{w}, \boldsymbol{v}, \boldsymbol{v}) + a(\boldsymbol{v}, \boldsymbol{w}) - b(\boldsymbol{w}, p) - b(\boldsymbol{v}, q) + s(\boldsymbol{v}, p, \boldsymbol{w}) \\ &= f(\boldsymbol{w}, \tilde{\boldsymbol{v}}) + f_c(\tilde{\boldsymbol{v}} - \boldsymbol{v}, \delta\tilde{\boldsymbol{v}}) \quad \forall \boldsymbol{w}, q, \delta\boldsymbol{t} \in V \times P \times Q \end{aligned} \tag{14}$$

where the involved bi- and tri-linear forms are defined as

$$a(\boldsymbol{v}, \boldsymbol{w}) = \int_\Omega \boldsymbol{\sigma}_d[\boldsymbol{v}] : \boldsymbol{l}[\boldsymbol{w}] \, dV \tag{15a}$$

$$b(\boldsymbol{v}, q) = \int_\Omega q \, \mathbf{1} : \boldsymbol{l}[\boldsymbol{v}] \, dV \tag{15b}$$

$$c(\boldsymbol{w}, \boldsymbol{u}, \boldsymbol{v}) = \int_\Omega \boldsymbol{w} \cdot (\boldsymbol{l}[\boldsymbol{u}] \cdot \boldsymbol{v}) \, (\rho dV) \tag{15c}$$

$$\left(\boldsymbol{w}, \boldsymbol{v}_{,t}\right) = \int_\Omega \boldsymbol{w} \cdot \boldsymbol{v}_{,t} \, (\rho dV) \tag{15d}$$

$$\begin{aligned} s(\boldsymbol{v}, p, \boldsymbol{w}) &= \int_\Omega \tau \, \boldsymbol{l}[\boldsymbol{w}] : (\boldsymbol{r} \otimes \boldsymbol{v}) \, dV \\ &= \sum_{e=1}^{\text{NEL}} \tau_e \int_{\Omega_e} \boldsymbol{l}[\boldsymbol{w}] : (\boldsymbol{r} \otimes \boldsymbol{v}) \, dV \end{aligned} \tag{15e}$$

The relations in Eqs. 14-15 constitute the coupled pressure-velocity problem of the material flow. As indicated in Fig. 1b, the Dirichlet boundaries are considered along Γ_v, the stress-free boundaries are considered along Γ_t, and the contact boundary is Γ_c. A special approach is used to reduce spurious oscillations in contact stresses as a result of a conventional regularized frictional/contact formulation, where contact velocities and stresses are of the same order of approximation. In the spirit of the developments in [17] to alleviate the violation of the inf-sup (LBB) condition for cohesive zone interfaces, a mixed weak formulation of the contact boundary is adopted to specify the stick/slip/separation along Γ_c for the flow problem. To this end, we introduced in Eq. 14 the coarse-grained contact velocity $\tilde{\boldsymbol{v}} \in C$, with $C = \{\bar{\boldsymbol{v}} \in L_2[\Gamma_c]\}$, as

$$f(\boldsymbol{w}, \tilde{\boldsymbol{v}}) = -\int_{\Gamma_c} \boldsymbol{w} \cdot \boldsymbol{t}[\tilde{\boldsymbol{v}}] \, dS \tag{16}$$

where the traction vector is completely determined by the coarse-grained velocity at the contact boundary. In addition, condition $\tilde{\boldsymbol{v}} \to \boldsymbol{v}$ is formulated in the weak sense so that

$$f_c(\boldsymbol{w}, \tilde{\boldsymbol{v}} - \boldsymbol{v}) = \int_{\Gamma_c} \mu_c \, (\tilde{\boldsymbol{v}} - \boldsymbol{v}) \cdot \delta\tilde{\boldsymbol{v}} dS = 0 \; \forall \delta\tilde{\boldsymbol{v}} \in C \tag{17}$$

where μ_c is a regularization parameter of highly irregular contact conditions along Γ_c. Further details of the stick/slip/separation formulation are given in "Tool-workpiece contact boundary" section.

In addition, standard SUPG stabilization $s(\boldsymbol{v}, p, \boldsymbol{w})$ is included in Eq. 14 in terms of the upwind weighting in the FE-discretized region and the residual of Eq. 12 written as

$$\boldsymbol{r}[\boldsymbol{v}, p] = \rho \left(\boldsymbol{v}_{,t} + \boldsymbol{l} \cdot \boldsymbol{v}\right) - (\boldsymbol{\sigma}_d \cdot \nabla - \nabla p) \tag{18}$$

SUPG stabilization becomes active in the convection-dominated NS avoiding numerical oscillations in the velocity field. In the present context, this may occur for high cutting speeds in conjunction with thermal softening that induces a reduced viscosity in the material. The details of the parameters involved are explained in "Details of the FE simulations" section.

Rheology of workpiece material

The deviatoric stress response in the modeled region is assumed to be non-Newtonian, where the pseudoplastic (or viscoplastic) part of the material response is based on the JC model. The rate of deformation tensor $\boldsymbol{d} = \boldsymbol{l}^{\text{sym}}$ is then divided into a viscoelastic part $\boldsymbol{d}^v$ and a viscoplastic part $\boldsymbol{d}^p$ so that $\boldsymbol{d} = \boldsymbol{d}^v + \boldsymbol{d}^p$, where the viscoelastic part defines the stress response through the viscous relation as

$$\boldsymbol{\sigma}_d = 2\mu\, \boldsymbol{I}_d : \boldsymbol{d}^v = 2\mu\, \boldsymbol{I}_d : (\boldsymbol{d} - \boldsymbol{d}^p) \tag{19}$$

where μ is the Newtonian shear viscosity parameter and $\boldsymbol{I}_d$ is the 4th order deviatoric projection operator. As for the viscoplastic part, we postulate

$$\boldsymbol{d}^p = \lambda \boldsymbol{f} \text{ with } \boldsymbol{f} = \nabla\phi = \frac{3}{2}\frac{\boldsymbol{\sigma}_d}{\sigma_e} \text{ and } \sigma_e = \sqrt{\frac{3}{2}}|\boldsymbol{\sigma}_d| \tag{20}$$

where $\phi := \sigma_e - g[\theta]\,(A + \kappa)$ is the yield function, σ_e is the von Mises effective stress, A is the initial yield stress, and κ is the microstress due to isotropic hardening. Furthermore, $\lambda \geq 0$ is the plastic multiplier determined by the JC-overstress function defined as

$$\lambda := \dot{\epsilon}_0 \exp\left[\frac{\langle\phi\rangle}{C g[\theta]\,(A+\kappa)}\right] \text{ if } \frac{\lambda}{\dot{\epsilon}_0} \geq 1 \tag{21}$$

where $\langle\phi\rangle$ denotes the positive part of ϕ. When $\frac{\lambda}{\dot{\epsilon}_0} < 1$, the rate-independent plastic response is controlled by loading conditions $\phi \leq 0$, $\lambda \geq 0$, $\phi\lambda = 0$. The parameters C and $\dot{\epsilon}_0$ control the rate sensitivity. These are degraded by thermal softening via the degradation function $g[\theta]$ defined as

$$g[\theta] = \begin{cases} 1 & \theta \leq \theta_t \\ 1 - \left(\frac{\theta-\theta_t}{\theta_m-\theta_t}\right)^m & \theta_t < \theta < \theta_m \\ 0 & \theta \geq \theta_m \end{cases} \tag{22}$$

For the JC model, the microhardening stress is $\kappa = Bk^n$ (B is the hardening parameter and n is the hardening exponent) in terms of the material hardening variable k, whose evolution is governed by the material time derivative as

$$\underbrace{(\nabla k)\cdot\boldsymbol{v} + k_{,t}}_{\dot{k}} = \lambda \tag{23}$$

Moreover, the evolution of temperature $\dot{\theta}$ is controlled by the energy equation

$$c_v \underbrace{\left((\nabla\theta)\cdot\boldsymbol{v} + \theta_{,t}\right)}_{\dot{\theta}} + \nabla\cdot\boldsymbol{q} = w^p - \left(\kappa + \theta\frac{\partial\kappa}{\partial\theta}\right)\lambda = \sigma_y\lambda \tag{24}$$

where $\boldsymbol{q}$ is the heat flux vector, the plastic work rate is $w^p = \sigma_e\lambda$ and $\sigma_y := \sigma_e - \kappa(g[\theta] + \theta g'[\theta])$.

The deviatoric stress response appears to be explicitly obtained in terms of the viscous (elastic) stress defined as $\boldsymbol{\sigma}_d^{\text{v}} := 2\mu\, \boldsymbol{I}_d : \boldsymbol{d}$. For viscoplastic loading $\phi[\sigma_e^{\text{v}}] > 0$, one obtains

$$\begin{aligned} \boldsymbol{\sigma}_d = 2\mu\boldsymbol{I}_d : \left(\boldsymbol{d} - \boldsymbol{d}^p\right) = \boldsymbol{\sigma}_d^{\text{v}} - 3\mu\lambda\frac{\boldsymbol{\sigma}_d}{\sigma_e} \\ \Rightarrow \boldsymbol{\sigma}_d\left(1 + \lambda\frac{3\mu}{\sigma_e}\right) = \boldsymbol{\sigma}_d^{\text{v}} \end{aligned} \tag{25}$$

The plastic multiplier can then be solved based on the sequel

$$\begin{aligned} \frac{\boldsymbol{\sigma}_d}{\sigma_e}(\sigma_e + \lambda 3\mu) = \sigma_e^{\text{v}}\frac{\boldsymbol{\sigma}_d^{\text{v}}}{\sigma_e^{\text{v}}} \Rightarrow \sigma_e = \sigma_e^{\text{v}} - \lambda 3\mu \Rightarrow \frac{\lambda}{\dot{\epsilon}_0} \\ = \exp\left[\frac{\sigma_e^{\text{v}} - \lambda 3\mu - (A+\kappa)}{C\,(A+\kappa)}\right] \end{aligned} \tag{26}$$

Hence, when the plastic multiplier is determined, $\sigma_e = \sigma_e^{\text{v}} - \lambda 3\mu$ is calculated, and the deviatoric stress tensor is evaluated as

$$\boldsymbol{\sigma}_d = \boldsymbol{\sigma}_d^{\text{v}} \begin{cases} 1 & \phi < 0 \\ \frac{\sigma_e}{\sigma_e^{\text{v}}} & \phi \geq 0 \end{cases} \tag{27}$$

The linearized viscous response is considered for fixed microhardening κ and temperature θ as

$$\delta\boldsymbol{\sigma}_d = \frac{\sigma_e}{\sigma_e^{\text{v}}}\delta\boldsymbol{\sigma}_d^{\text{v}} + \frac{2}{3}\left(\delta\sigma_e - \frac{\sigma_e}{\sigma_e^{\text{v}}}\delta\sigma_e^{\text{v}}\right)\boldsymbol{f}^{\text{v}} \text{ with } \boldsymbol{f}^{\text{v}} = \frac{3}{2}\frac{\boldsymbol{\sigma}_d^v}{\sigma_e^v} \tag{28}$$

where $\delta\boldsymbol{\sigma}_d^{\text{v}} = 2\mu\boldsymbol{I}_d : \delta\boldsymbol{d}$ and $\delta\sigma_e^{\text{v}} = 2\mu\boldsymbol{f}^{\text{v}} : \delta\boldsymbol{d}$. It also follows that $\delta\sigma_e = \delta\sigma_e^{\text{v}} - 3\mu\delta\lambda$ and

$$\log\left[\frac{\lambda}{\dot{\epsilon}_0}\right] = \frac{\sigma_e^{\text{v}} - \lambda 3\mu - (A+\kappa)}{C\,(A+\kappa)} \rightsquigarrow \delta\lambda = a\,\delta\sigma_e^{\text{v}} \tag{29}$$

with

$$a = \frac{\lambda}{3\mu\lambda + C\,(A+\kappa)} \tag{30}$$

Then $\delta\sigma_e = (1 - 3\mu a)\delta\sigma_e^{\text{v}} = (1 - 3\mu a)2\mu\boldsymbol{f}^{\text{v}} : \delta\boldsymbol{d}$ is obtained in viscoplastic loading. Hence, it is obtained that $\delta\boldsymbol{\sigma}_d = \boldsymbol{D} : \delta\boldsymbol{d}$ where the viscous modulus tensor of the stress response is

$$\boldsymbol{D} = 2\mu \begin{cases} \boldsymbol{I}_d & \phi < 0 \\ \frac{\sigma_e}{\sigma_e^{\text{v}}}\boldsymbol{I}_d + \frac{2}{3}\left(1 - 3\mu a - \frac{\sigma_e}{\sigma_e^{\text{v}}}\right)\boldsymbol{f}^{\text{v}} \otimes \boldsymbol{f}^{\text{v}} & \phi \geq 0 \end{cases} \tag{31}$$

Weak forms of hardening and temperature evolution

In the Eulerian formulation, the evolution of the material hardening variable $k = k[\boldsymbol{x}, t] \geq 0$ is governed by the convection problem of Eq. 23 as

$$r_k = (\nabla k) \cdot \boldsymbol{v} + k_{,t} - \lambda = 0 \; \forall \boldsymbol{x} \in \Omega \tag{32}$$

Here, λ is given from the momentum balance and the constitutive problem in the sequel (20)-(23). A stabilized weak form of Eq. 23 is written as

$$((\nabla k)\cdot \boldsymbol{v}, \gamma) + \big(k_{,t}, \gamma\big) + s(k, \gamma) + r_p(\langle k \rangle_-, \gamma) = (\lambda, \gamma) \; \forall \gamma \in S \tag{33}$$

where no boundary conditions for $k-$values are needed. Similarly to the momentum and mass conservation of the NS equations, upwind stabilization is used in terms of the residual r_k defined as

$$s(\boldsymbol{v}; k, \gamma) = \sum_{e=1}^{\text{NEL}} \tau_e \, (r_k[k, t], (\nabla \gamma) \cdot \boldsymbol{v})_{\Omega_e} \tag{34}$$

where the elemental stabilization time is $\tau_e = h_e/|\boldsymbol{v}|$ [27]. Furthermore, to avoid solutions $k < 0$, the penalty term $r_p \langle k \rangle_-$ is introduced in Eq. 33 in terms of the negative part function $\langle \bullet \rangle_-$. In the present application, we have found that the penalty parameter $r_p = 1000 - 2000$ is a suitable numerical choice.

As to the energy equation (24), it is restated in residual form as

$$r_\theta = c_v \left((\nabla \theta) \cdot \boldsymbol{v} + \theta_{,t} \right) + \nabla \cdot \boldsymbol{q} - \sigma_y \lambda = 0 \; \forall \boldsymbol{x} \in \Omega \tag{35}$$

The weak form including stabilization and Fouriers law $\boldsymbol{q} = -k_c \nabla \theta$, where k_c is the thermal conductivity, is

$$c(\boldsymbol{v}; \chi, \theta) + (\chi, \theta_{,t}) + a(\chi, \theta) + s(\boldsymbol{v}; \chi, \theta) - f(\chi, \theta) = 0 \; \forall \chi \in S \tag{36}$$

where

$$c(\boldsymbol{v}; \chi, \theta) = \int_\Omega \chi \, (\nabla \theta) \cdot \boldsymbol{v} \, (c_v dV) \tag{37a}$$

$$\big(\chi, \theta_{,t}\big) = \int_\Omega \chi \, \theta_{,t} \, (c_v dV) \tag{37b}$$

$$a(\chi, \theta) = \int_\Omega (\nabla \chi) \cdot (\nabla \theta) \, (k_c dV) \tag{37c}$$

$$s(\boldsymbol{v}; \chi, \theta) = \int_\Omega \tau \, r_\theta \, (\nabla \chi) \cdot \boldsymbol{v} \, dV = \sum_{e=1}^{\text{NEL}} \tau_e \int_{\Omega_e} r \, (\nabla \chi) \cdot \boldsymbol{v} \, dV \tag{37d}$$

$$f(\chi, \theta) = \int_\Omega \chi \, \sigma_y[\theta] \lambda \, dV - \int_\Gamma \chi \, q_{n_c} \, dS \tag{37e}$$

Tool-workpiece contact boundary

Regarding mechanical boundary conditions, stress-free boundaries are defined along Γ_t, while the Dirichlet boundary is applied along Γ_v for the subscale field $\boldsymbol{v}^s$. Since $\boldsymbol{v}^s = \boldsymbol{0}$ along Γ_v, the workpiece is subjected to the cutting speed v_c due to the DPZD approximation. To express the mechanical response of the tool-workpiece contact boundary Γ_c, the mechanical contact interface is considered in Fig. 3 showing the response of the contact interface to material flow. Hence, the normal stress (or contact pressure $p = -\sigma_n = -\boldsymbol{n_c} \cdot \boldsymbol{t}$) is $\boldsymbol{t}_{n_c} = \sigma_n \boldsymbol{n_c}$ and the contact shear is $\boldsymbol{\tau}$, which defines the contact traction vector as $\boldsymbol{t} = \boldsymbol{t}_{n_c} + \boldsymbol{\tau}$. A non-Newtonian contact response is also introduced in terms of the regularization parameter μ_c and the regularized normal slip $\boldsymbol{v} - \boldsymbol{v}_s \to \boldsymbol{0}$ for $\mu_c \to \infty$. This is defined as

$$\boldsymbol{t} = \mu_c (\boldsymbol{v} - \boldsymbol{v}_s) \tag{38}$$

where $\boldsymbol{v}_s$ is the slip velocity. Here, the regularization parameter is related to a geometric measure of the cutting zone through the bulk viscosity and the relation $\mu_c = \mu/\delta$, where the geometric measure δ is typically chosen as a small value $\delta = 10^{-6}$mm. Note that in this section we use the notation $\boldsymbol{v}$ for the contact velocity for brevity, while in the weak form (16) we adopt the coarse-grained velocity $\tilde{\boldsymbol{v}}$ when calculating the traction vector.

Moreover, upon introducing the normal and shear projection operators $\mathbf{1}_{n_c} = \boldsymbol{n_c} \otimes \boldsymbol{n_c}$ and $\mathbf{1}_s = \mathbf{1} - \boldsymbol{n_c} \otimes \boldsymbol{n_c}$, respectively, the contact traction vector in the normal and shear components is formulated as

$$\begin{aligned} &\boldsymbol{t} = \boldsymbol{t}_{n_c} + \boldsymbol{\tau} \text{ with } \boldsymbol{t}_{n_c} = \mu_c \mathbf{1}_{n_c} \cdot \boldsymbol{v} \, , \\ &\boldsymbol{\tau} = \boldsymbol{\tau}^v - \mu_c \boldsymbol{v}_s \text{ and } \boldsymbol{\tau}^v = \mu_c \mathbf{1}_s \cdot \boldsymbol{v} \end{aligned} \tag{39}$$

where $\boldsymbol{\tau}^v$ is the Newtonian contact shear stress in stick loading. For the slip velocity, the friction function ϕ_s of the Mohr-Coulomb type is introduced as

$$\phi_s = |\boldsymbol{\tau}| + f[\sigma_n] \leq 0 \tag{40}$$

where $f[\sigma_n]$ represents the crucial stick/slip friction behavior of the tool-workpiece contact interface. We consider the classical Mohr-Coulomb friction law in the friction parameter γ_c defined as

$$f[\sigma_n] = \gamma_c \sigma_n \text{ with } f'[\sigma_n] = \gamma_c \tag{41}$$

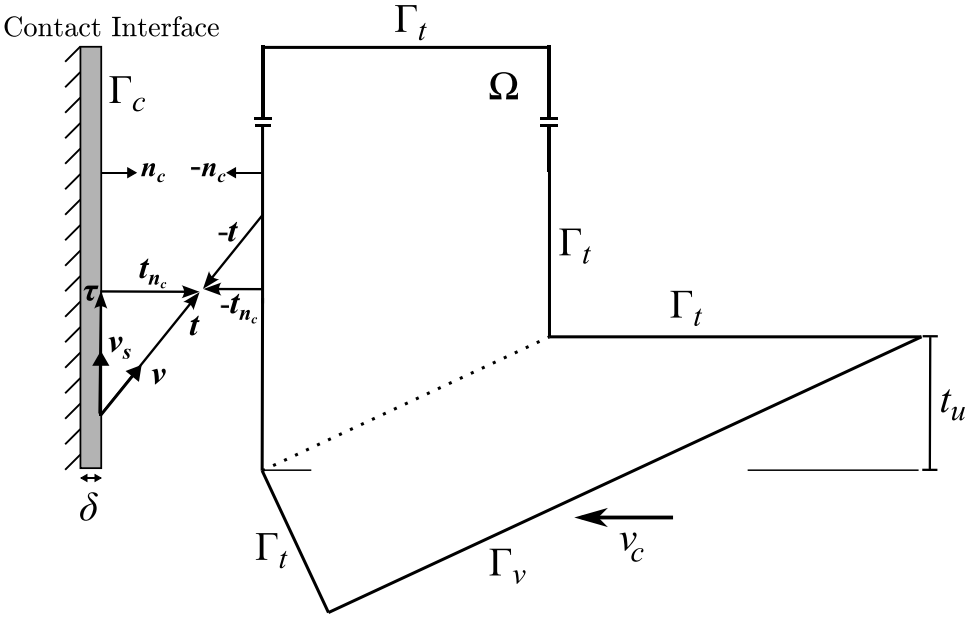

Fig. 3 Mechanical contact interface to manage regularized stick/slip/separation contact using the regularization parameter δ. Note that the contact traction vector $\boldsymbol{t}$ represents the reactive contact stresses on the workpiece material

The material slip is defined by

$$\boldsymbol{v}_s = \lambda \frac{\partial \phi_s}{\partial \boldsymbol{\tau}} = \lambda \boldsymbol{g} = \lambda \frac{\boldsymbol{\tau}}{|\boldsymbol{\tau}|} \text{ with } \phi_s \leq 0\,,\, \lambda \geq 0\,,\, \phi_s \lambda = 0 \tag{42}$$

From the constitutive interface relation, in slip loading $\lambda > 0$, $\boldsymbol{\tau}$ is obtained as

$$\boldsymbol{\tau} = \mu_c \left(\mathbf{1}_s \cdot \boldsymbol{v} - \boldsymbol{v}_s\right) = \boldsymbol{g}^v |\boldsymbol{\tau}^v| - \lambda \mu_c \boldsymbol{g} \tag{43}$$

which yields

$$\boldsymbol{g}\left(|\boldsymbol{\tau}| + \lambda \mu\right) = \boldsymbol{g}^v \left|\boldsymbol{\tau}^v\right| \Rightarrow \boldsymbol{g} = \boldsymbol{g}^v \text{ and } |\boldsymbol{\tau}| = |\boldsymbol{\tau}^v| - \lambda \mu_c \tag{44}$$

From the slip loading, the friction function is derived as

$$\begin{aligned} \phi_s &= |\boldsymbol{\tau}| + f[\sigma_n] = \underbrace{|\boldsymbol{\tau}^v| + f[\sigma_n]}_{\phi_s^v} - \lambda \mu_c \\ &= 0 \Rightarrow \lambda = \frac{\phi_s^v}{\mu_c} \geq 0 \end{aligned} \tag{45}$$

where ϕ_s^v is the Newtonian interface loading function. For the interface law, separation and stick/slip are distinguished as

$$\sigma_n = \mu_c v_n \geq 0 \Rightarrow \boldsymbol{t} = \boldsymbol{t}_{n_c} = \boldsymbol{\tau} = \mathbf{0} \text{ (separation)} \tag{46}$$

The stick/slip condition is indicated whenever $\sigma_n = \mu_c v_n < 0$. In this condition, the different cases are obtained depending on the sign of the loading function ϕ_s^v as

$$\frac{\phi_s^v}{\mu_c} \leq 0\,,\, \boldsymbol{v}_s = \mathbf{0} \Rightarrow \boldsymbol{t} = \boldsymbol{t}_{n_c} + \boldsymbol{\tau}^v = \mu_c \boldsymbol{v} \text{ (stick)} \tag{47a}$$

$$\begin{aligned} \lambda = \frac{\phi_s^v}{\mu_c} > 0\,,\, \boldsymbol{v}_s = \frac{\phi_s^v}{\mu_c} \boldsymbol{g}^v \\ \Rightarrow \boldsymbol{t} = \boldsymbol{t}_{n_c} + \boldsymbol{\tau}^v - \phi_s^v \boldsymbol{g}^v = \mu_c \boldsymbol{v} - \phi_s^v \boldsymbol{g}^v \text{ (slip)} \end{aligned} \tag{47b}$$

Linearization in stick/slip loading is obtained as $\delta \boldsymbol{t} = \boldsymbol{D}_c \cdot \delta \boldsymbol{v}$, leading to

$$\boldsymbol{D}_c = \mu_c \begin{cases} \mathbf{1} & \phi_s^v \leq 0 \\ \mathbf{1} - \boldsymbol{g}^v \otimes \boldsymbol{g}^v - f' \boldsymbol{g}^v \otimes \boldsymbol{m} & \\ \quad - \frac{\phi_s^v}{|\boldsymbol{\tau}^v|} (\mathbf{1}_s - \boldsymbol{g}^v \otimes \boldsymbol{g}^v) & \phi_s^v > 0 \end{cases} \tag{48}$$

where $\boldsymbol{D}_c$ is the second-order contact interface stiffness.

For the thermal part of the contact boundary, the initial temperature is set to $\theta_i = 25°\text{C}$ throughout the region Ω. In the stick/slip contact region of Γ_c, with contact length l_c, heat generation is responsible for both deformation in Ω and contact friction along Γ_c. Firstly, the heat partition to the tool R_T is calculated by using Berliner and Krajnov's relation [28] as

$$R_T = \frac{0.45(k_T/k_W)\sqrt{\pi \alpha_W / (v_{ch} l_c)}}{1 + 0.45(k_T/k_W)\sqrt{\pi \alpha_W / (v_{ch} l_c)}} \tag{49}$$

where k_T/k_W denotes the ratio of the thermal conductivities between the tool and the workpiece materials, α_W is the thermal diffusivity of the workpiece material, and v_{ch} is the

chip velocity. The thermal diffusivity is calculated as

$$\alpha_W = \frac{k_c}{\rho c_p} \text{ with } \rho c_p = c_v \tag{50}$$

where k_c is the thermal conductivity, ρ is the density and c_p is the specific heat capacity of the workpiece material. The chip velocity can be calculated from the cutting speed v_c and the shear angle φ as

$$v_{ch} = v_c \tan\varphi \tag{51}$$

The heat partition R_T represents the amount of total heat that is transferred to the tool, which consequently exits the system through the contact region Γ_c. Thus, the R_T-portion of the total heat generation from the deformation q_{def} and friction q_{fric} is later applied to Γ_c as heat loss. Moreover, the $(1 - R_T)$ portion of q_{fric} remains in the system, which is applied as a heat source along Γ_c. Thus, the heat flux q_{n_c} in the n_c direction (see Fig. 1b) along Γ_c can be stated as

$$q_{n_c} = R_T(q_{fric} + q_{def}) - (1 - R_T)q_{fric} \tag{52}$$

Solution procedure

To handle the solution in terms of momentum/mass balance (14), the DPZD solution (2), the convective hardening problem (33) and the temperature evolution problem (36), a staggered solution procedure is adopted. At first, the geometry is created according to the DPZD assumptions. DPZD model uses experimental measurements and cutting condition parameters to determine the PSZ region that is created based on the uncut chip thickness (feed) t_u, the shear angle φ, and the thickness b of the PSZ. The parameters b and φ are calculated from Eq. 8. It is important to mention that even though the DPZD model requires experimental data, estimation tools, which are based on empirical and/or analytical models, may also be used to supply the required input data for the geometry of the PSZ region. Furthermore, to model the cutting process and obtain a stable solution procedure, the cutting speed increases linearly in the simulations with the number of time steps $mtim$ in time, leading to $v_c[t] = \frac{t}{T} v_c$ where T is the total time and v_c is the given cutting speed. The procedure is described as follows:

1. For all time steps, itim=1:mtim
2. Given the thickness of the shear zone b, the shear angle φ, the rake angle β and the cutting velocity $v_c[t]$, calculate the long-range velocity field $\bar{\boldsymbol{v}}[\boldsymbol{x}]$ from the DPZD approximation (2) with r =4.
3. Given the hardening and temperature fields $k[\boldsymbol{x}]$ and $\theta[\boldsymbol{x}]$, calculate the subscale velocity $\boldsymbol{v}^s[\boldsymbol{x}]$, the pressure field $p[\boldsymbol{x}]$ and the (Lagrange) traction field $\boldsymbol{t}[\boldsymbol{x}]$ from the FE-discretization in the stabilized momentum and mass balance relations contained in Eq. 14. Compute and deliver at the Gauss point level the plastic multiplier λ, effective stress σ_e, and microhardening stress κ.
4. Given the plastic multipliers λ from Step 3, calculate the material hardening field $k[\boldsymbol{x}]$ from the weakly stabilized form of the hardening evolution (33). At the element level, the mean value $\lambda_e =< \lambda >$ of the Gauss points is used.
5. Given the plastic multipliers at the element level λ_e, the effective von Mises stresses σ_e and the microhardening κ_e from Step 3, calculate the temperature field $\theta[\boldsymbol{x}]$ from the weak form of the thermal evolution problem (36).
6. Go to Step 1

Machining experiments and FE simulations

In this section, the specifics of the machining experiment considered for orthogonal cutting and details of the FE simulations, based on the Eulerian subscale model and the commercial software DEFORM 2D employing the Lagrangian approach, are described. The parameter identification considered for the subscale model is also included in this section.

Experimental details

In orthogonal cutting, the effect of the depth of cut (i.e. out-of-plane direction) is very small, and the passive force is close to zero. Therefore, orthogonal cutting experiments are suitable validation cases to observe the performance of the presented 2D subscale model. Detailed information on the experimental procedure and the measured values is given in a previous publication [29]. As stated in the reference, orthogonal cutting experiments are performed for C38 steel under dry cutting conditions. The C38 steel workpiece material, whose chemical composition is given in Table 1, is taken directly from a crankshaft component.

Table 1 The chemical composition of C38 steel

C%	Si%	Mn%	P%	S%
0.35 – 0.40	0.45 – 0.65	1.30 – 1.50	< 0.025	0.018 – 0.033
Cr%	V%	Al%	Cu%	N%
0.20 – 0.30	0.08 – 0.12	0.005 – 0.030	<0.35	0.0090 – 0.0200

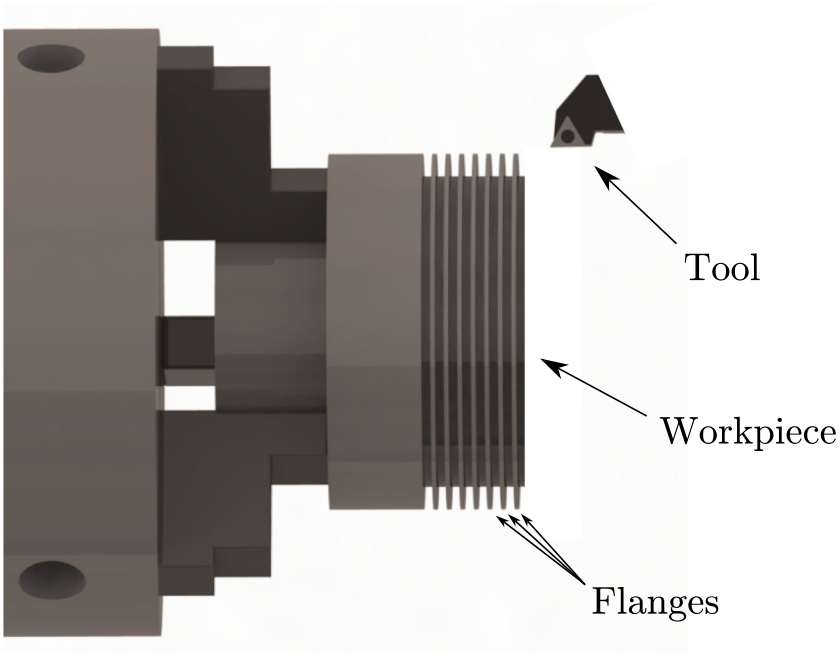

Fig. 4 Representation of the experimental setup for orthogonal cutting

To ensure orthogonal conditions, several flanges (approximately $2mm$ thick) are fabricated and then machined in the radial direction on the workpiece. The cutting operation is performed on an EMCO 365 CNC lathe connected to a Kistler 9275A three-component dynamometer for force measurements. The tools used in the experiments are Sandvik Coromant H13A uncoated cemented carbide TCMW16T304 inserts without a chip breaker. The tools are mounted in the tool holder with 0° rake angles and 7° clearance angles. A representation of the experimental setup can be seen in Fig. 4.

Based on the experimental data given in [29], three cutting conditions are selected to evaluate the performance of the subscale model, where the cutting speed v_c and feed t_u change, while the depth of cut a_p is constant. These three cutting conditions are selected to reflect the effect of varying the cutting speed and feed in the simulations and to observe the performance of the simulations toward these changes. The cutting conditions are given in Table 2, including the measured cutting force F_c and the feed force F_f.

Details of the FE simulations

After the geometry for the *subscale flow model* is defined, FE discretization is performed. Approximately 2000 six-noded triangular Taylor-Hood elements (with a quadratic velocity and linear pressure approximation) are used in the subscale flow model to avoid spurious oscillations in the pressure field. Here, the element-wise streamline diffusion time (or stabilization) parameter τ_e in Eq. 15e is defined [27, 30] as

$$\tau_e = h_e \left(|\boldsymbol{v}|^2 + 2 \left(\frac{h_e}{\Delta t} \right)^2 + 60 \left(\frac{\nu}{h_e} \right)^2 \right)^{-\frac{1}{2}} \tag{53}$$

where Δt is the time step size, h_e is the element diameter and $\nu = \mu/\rho$ is the kinematic viscosity. In terms of time steps, the cutting speed increases linearly with $\bar{v}_c[t] = t/T v_c$. We choose $T = 0.1$s to arrive using 3000 time steps in a steady state of the flow conditions for all cutting conditions. The viscoplastic flow parameters of the workpiece material are identified from the calibration procedure discussed in "Parameter calibration" section. In this development, the Newtonian shear viscosity parameter is $\mu = 1\text{Ns/mm}^2$. In order to resolve the stick/slip/separation conditions of the contact boundary, smaller elements are used in the vicinity of Γ_c. In particular, it is necessary to properly resolve the stick region close to the tool tip. For interpolation of fine-grained contact velocity $\boldsymbol{v} \in \Gamma_c$, the associated *quadratic* FE interpolation of Taylor-Hood elements is used, while for

Table 2 Cutting Conditions of Orthogonal Cutting Experiments

Experiment	$v_c\ (m/min)$	$t_u\ (mm/rev)$	$a_p\ (mm)$	$F_c\ (N/mm)$	$F_f\ (N/mm)$
O1	180	0.075	1.95	230	188
O2	240	0.050	1.95	166	139
O3	240	0.075	1.95	224	186

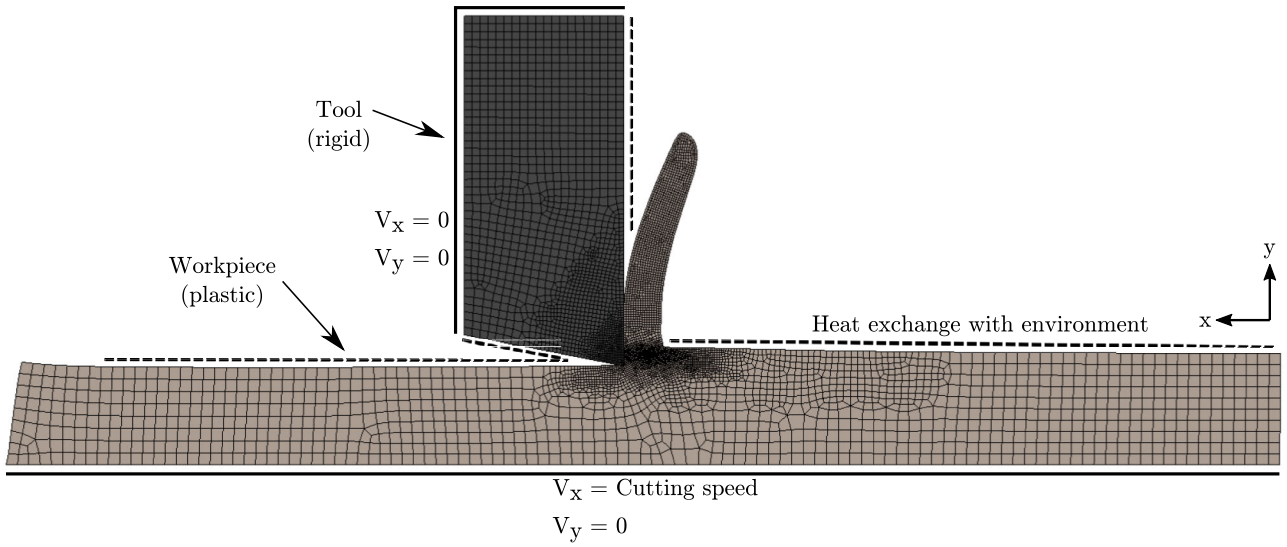

Fig. 5 DEFORM 2D simulation setup for orthogonal cutting

the course-grained velocity $\tilde{\boldsymbol{v}} \in \Gamma_c$, only the corner nodes of Taylor-Hood elements are enabled using linear interpolation.

In addition to the experimental validation, the performance of the subscale model is further evaluated by comparing it with FE chip formation simulations performed in DEFORM 2D. For comparison, a Lagrangian simulation employing the FE software SFTC DEFORM 2D^{TM} is considered. For this case, quadrilateral elements are used for both the workpiece and the tool with a minimum element size of 0.005mm. The simulation setup with applied boundary conditions is shown in Fig. 5. In the setup, the tool is fixed, while the cutting speed is applied in the x direction at the bottom of the workpiece material according to Table 2.

For the mechanical part, the workpiece material is elastic-viscoplastic, where the viscoplasticity is represented by the identical JC model outlined herein. The JC parameters, which were calibrated in a previous study [29], are shown in Table 3. For the tool-workpiece contact, a pressure-dependent shear friction model from [31] is used as

$$\tau = (1 - \exp[-0.0045\, p]) \frac{A}{\sqrt{3}} \tag{54}$$

where τ is the shear stress at the contact interface, $A/\sqrt{3}$ represents the shear strength of the workpiece and p is the contact pressure at the interface. To reduce computational effort, the tool is assumed to be rigid in the simulation.

For the thermal part, heat exchange in the environment is defined by the heat transfer coefficient of 0.2kW/m^2°C, which refers to forced air heat convection, while the ambient temperature is set to 25°C. The heat transfer coefficient between the tool and the workpiece is 10^5kW/m^2°C, a commonly used parameter for machining simulations [31–33]. The thermal conductivity and heat capacity for the workpiece material for both models are shown in Table 4.

Parameter calibration

To calibrate the material behavior for the subscale model, simulation-based parameter identification is performed. 20 sets of parameters A, B, n, C, and m were randomly selected to perform subscale model simulations for each set for cutting condition O1 in Table 3. To reduce total computational time, the simulations were performed with a coarser mesh (with 300 triangular elements) using the same number of time steps ($mtim$ = 3000). Moreover, for the contact behavior, the classical Mohr-Coulomb friction law uses a high friction coefficient to ensure that only sticking occurs and there is no sliding. To avoid overestimation of the cutting forces, the JC parameters are identified for the case with the highest cutting force, since the cutting force increases with increasing friction coefficient [34]. In parameter identification, the cutting force F_c and the feed force F_f are collected from the simulations. The sets of JC parameters and forces are used in a

Table 3 Johnson-Cook parameters for C38 steel for the 1) the Lagrangian approach [29] and 2) the calibrated parameters for the Eulerian subscale flow model

Type	A (MPa)	B (MPa)	C	n	m	$\dot{\epsilon}_0$ (1/s)	θ_m (°C)
DEFORM 2D	589	145	0.25	0.069	1.1	1	1460
Subscale model	745	328	0.095	0.058	1.08	1	1460

Table 4 Thermal parameters for the models; DEFORM 2D (temperature dependent) and subscale (constant)

Property	DEFORM 2D [29]	Subscale model
k_c (W/m°C)	$(1.645\times10^{-5})\theta^2 - (0.0321)\theta + 45.1088$	39.6
c_p (J/g°C)	$(1.707\times10^{-9})\theta^3 - (3.653\times10^{-6})\theta^2 + (0.0025)\theta + 0.2306$	0.456

minimization algorithm that reduces the difference between the estimated and experimental measured forces in Table 2. The identified JC parameters with minimum deviation are given in Table 3.

Model validation

In this section, the subscale model is validated by comparison with experimental data and DEFORM 2D simulations. The robustness and efficiency aspects of the subscale model are emphasized in comparison to the commonly used chip formation simulations. Verification of the stability of the response at the contact boundary is also performed using the mixed method. The validations focus on the cutting and feed forces, as well as the distributions of stress and temperature. Forces offer insight into the overall performance of the models, while stress and temperature distributions provide a detailed view, reflecting the accuracy of the model in the shear zones. In addition, the behavior of contact within the model and the influence of the cutting speed on the results are examined. In the subscale model simulations, the calibrated JC parameters (see Table 3) are used. For the contact boundary, the classical Mohr-Coulomb friction with friction coefficient $\gamma_c = 0.5$ is considered.

Stress oscillations at the contact boundary

To verify the mixed method for the tool-workpiece contact interface, the proposed quadratic/linear approximation of $\boldsymbol{v},\ \tilde{\boldsymbol{v}} \in \Gamma_c$ is compared with the quadratic/quadratic approximation, which is similar to the standard displacement-based approach employed for standard regularized contact elements. Figure 6 shows the resulting normal and tangent components of contact stress at the final load step for cutting condition O3. Severe unwanted stress oscillation is obtained for both stress components when using the quadratic approximation of the coarse-grained contact velocity $\tilde{\boldsymbol{v}}$. When using the linear approximation for $\tilde{\boldsymbol{v}}$ and the quadratic approximation for $\boldsymbol{v}$, the stress oscillation is significantly diminished, as observed in Fig. 6.

Cutting forces

In Fig. 7, the measured cutting and feed forces are compared with the predictions of both the DEFORM 2D simulations and the subscale model. In terms of cutting force, both models slightly overestimate the experimental measurements for all cutting conditions. The subscale model has the smallest deviation. For the feed force, both models significantly underestimate the experiments. The largest deviation in feed force

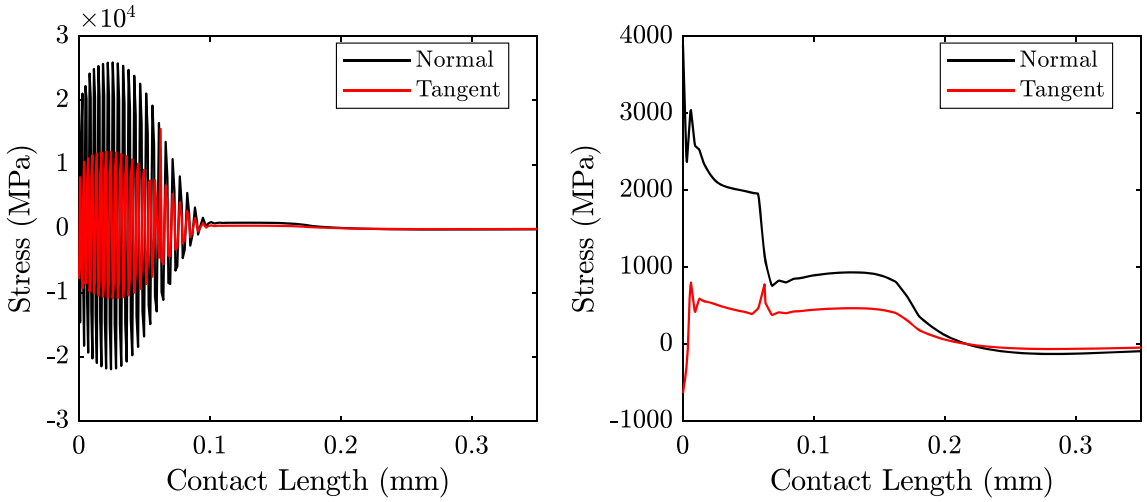

Fig. 6 Behavior of contact stresses following the classical Mohr-Coulomb friction model at integration points along the contact length of Γ_c for the cutting condition O3. (left) Unstable oscillating behavior for the quadratic approximation for $\tilde{\boldsymbol{v}}$ and $\boldsymbol{v}$. (right) Stabilized behavior when using the linear approximation for $\tilde{\boldsymbol{v}}$ and the quadratic approximation for $\boldsymbol{v}$

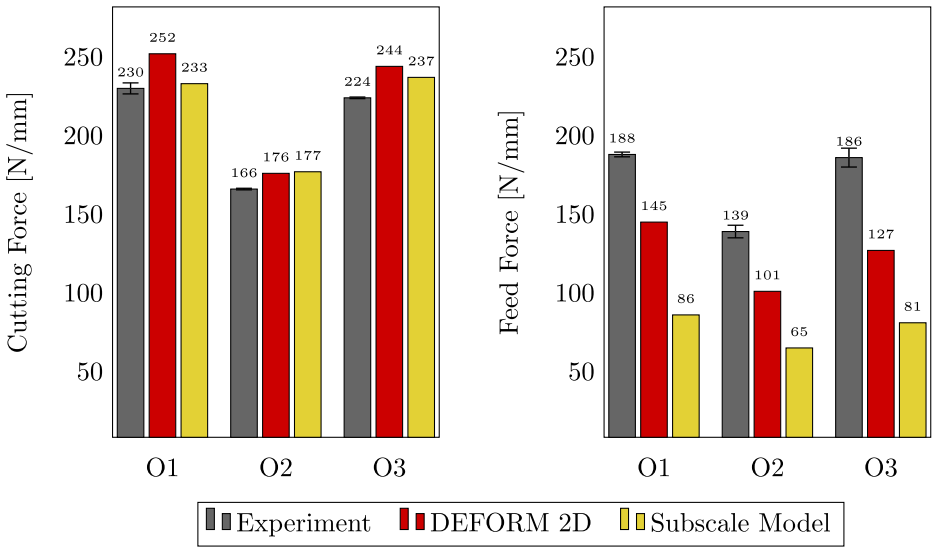

Fig. 7 Cutting and feed forces obtained from orthogonal cutting experiments (O1-O3) [29], DEFORM 2D simulations [29] and the subscale model

is 56% for the subscale model in the O3 condition. Likewise, the DEFORM 2D simulation underestimates the feed forces with the 32% largest deviation under the O3 condition.

It should be noted that an increase in the feed from O2 to O3 (that is, from 0.050 to 0.075mm/rev) is expected to increase both the cutting and the feed forces. Although the magnitude varies, the trend of increasing cutting and feed forces is consistently obtained in both the DEFORM 2D and subscale models. Furthermore, an increase in cutting speed from O1 to O3 (that is, 180 to 240 m / min) exhibits a slight reduction in both cutting and feed forces. The DEFORM 2D simulation successfully captures this trend for both forces. When comparing the O1 to O3 conditions for the subscale model, there is a slight increase in the cutting force, while the feed force is decreasing slightly. This may be attributed to the DPZD assumptions used in defining the discretized region. Incorporating a friction model that accounts for pressure or velocity dependence could also potentially produce more accurate results and better reflect these observed trends [35].

Stress and temperature distributions

To evaluate the predictive performance of the subscale model, the stress and temperature distributions obtained from this model are compared with those obtained from DEFORM 2D and DPZD, as shown in Figs. 8 and 9. It is important to note that the DPZD model exclusively considers the central region of the PSZ and does not account for variations along the shear line depicted in Fig. 1b. When examining the stress distributions in Fig. 8, differences are observed in the location of the maximum stress between the models. The DPZD model assumes that the maximum stress occurs along the shear line, whereas the DEFORM 2D simulation indicates that it is slightly below the shear line. This difference may be attributed to the assumption of a perfectly sharp tool in the DPZD model. However, the subscale model, which also assumes a perfectly sharp tool (similar to the DPZD model), exhibits the maximum stress occurring below the shear line. This suggests that an additional factor may be influencing the results, hypothetically the stagnation region near the tip

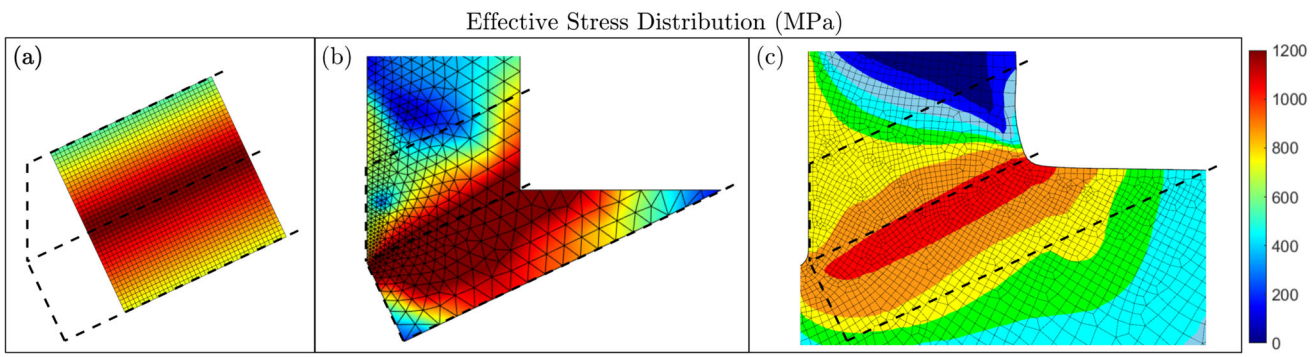

Fig. 8 Effective stress distribution from (a) the DPZD model, (b) the subscale model, and (c) DEFORM 2D for the cutting condition O3

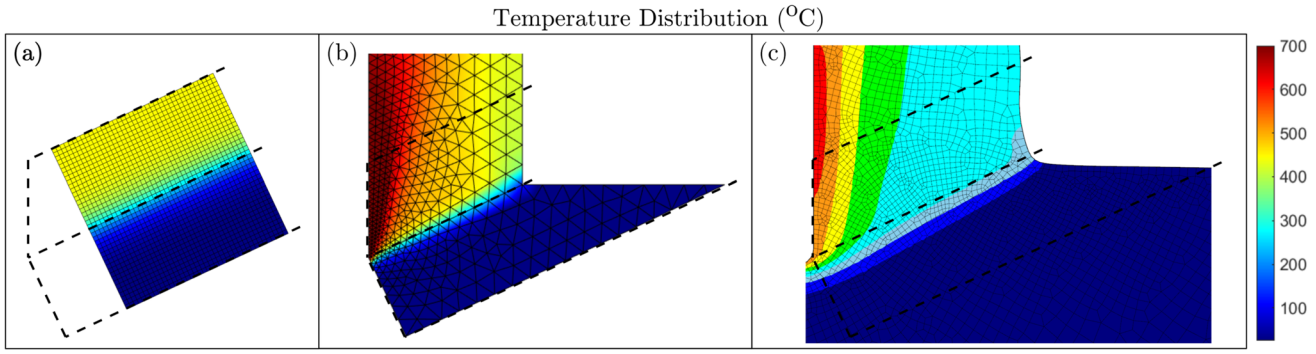

Fig. 9 Temperature distribution of (a) the DPZD model, (b) the subscale model, and (c) DEFORM 2D for the cutting condition O3

of the tool, where material movement is minimal and stress levels are lower compared to the high-deformation response along the shear line. When comparing the subscale model to DEFORM 2D, the stress distribution within the PSZ is consistent with the location of the maximum stress region, the distribution around the contact area, the stress increase from the material side to the shear line and the subsequent decrease towards the chip side of the primary zone. It should be noted that the maximum stresses predicted by the subscale model are higher (approximately 1450MPa) compared to the DEFORM 2D simulation (approximately 1230MPa). This difference is likely due to differences in material parameters between the models, leading to variations in the hardening behavior of the material. Furthermore, effective stress distributions remain very similar under different cutting conditions (from O1 to O3), with only a slight variation of 1-2% in maximum values.

The temperature distributions depicted in Fig. 9 appear similar, except the DPZD distribution, which focuses solely on the central region of the PSZ and disregards the effect of the contact area, where the maximum temperature is reached due to friction. When comparing the subscale model to DEFORM 2D, notable differences are observed in the temperature distributions near the contact region. These differences arise because a simplified heat flux based on the heat partition approach is applied in the subscale model, while the heat flux from the chip to the tool exhibits a more complex distribution [36, 37].

The maximum temperatures predicted by the subscale model and the DEFORM 2D model are approximately 1050°C and 750°C, respectively. According to a study conducted under similar material and cutting conditions (i.e., 200m/min cutting speed and 0.1mm feed) [38], the maximum temperature was measured in the range between 770°C and 940°C. The subscale model presented here overestimates the maximum temperature compared to this reference range. However, it is important to note that the thermal interface and heat transfer to the tool within the subscale model require improvement to improve the accuracy of the temperature predictions. Taking into account the other cutting conditions (O1 and O2), the temperature distribution remains similar to that

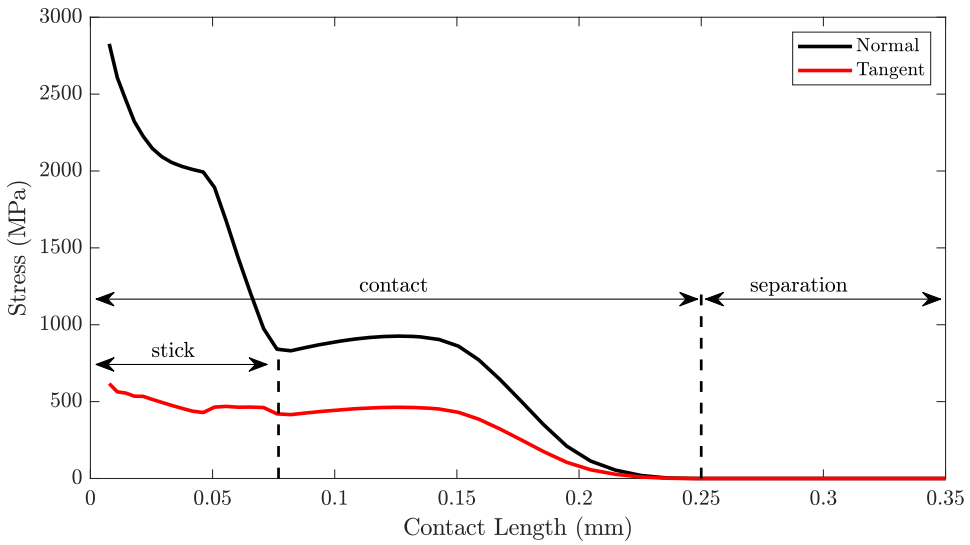

Fig. 10 Stress distribution over the contact length obtained from the subscale model with cutting condition O3

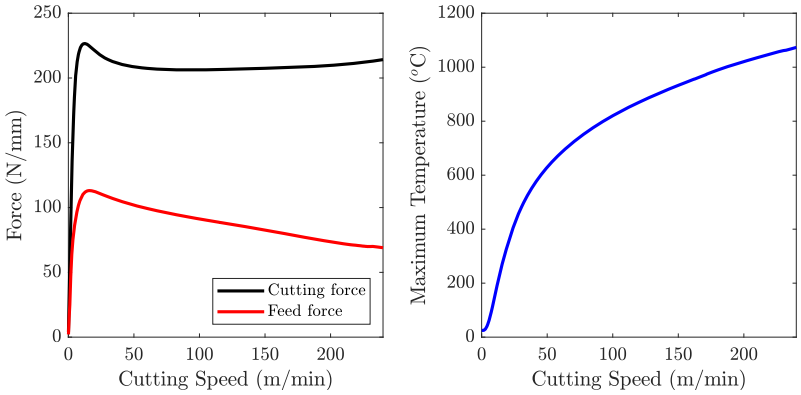

Fig. 11 Forces and maximum temperature response based on linear increase in cutting speed. Data are collected from the simulation of the cutting condition O3

shown in Fig. 9(b), with differences in maximum temperatures of 1000°C and 1020°C, respectively.

Contact behavior

The tool-workpiece contact behavior, where the material undergoes maximum deformation and heat generation, is crucial for accurately estimating cutting forces. To validate this behavior, the normal and tangential stresses distributed along the contact length are derived from the traction field on the contact length Γ_c, assuming both stick and slip conditions. These stress distributions are presented in Fig. 10. As illustrated, the normal stress decreases along the contact length, while the tangential component remains relatively the same on most of the contact. The oscillations observed near the start of the contact length are attributed to the material flow from the corner elements and can be ignored.

The normal stress distribution illustrated in Fig. 10 allows the identification of the stick, slip, and separation regions. A sudden change in normal stress from a decrease to an increase signals a shift from the stick state to the slip state within the elements. Further along the contact length, the normal stress decreases to zero, indicating the point at which the chip separates from the tool. The contact behavior predicted by the subscale model aligns with the findings in the existing literature. For instance, Malakizadi et al. [39] report a similar pattern for the pressure-dependent shear friction model.

Cutting speed-dependent forces and temperature

As mentioned in the simulation of the cutting process using the subscale model, the cutting velocity is linearly increased until the material flow stabilizes in the desired steady-state condition when the total analysis time has been reached. Based on the data collected at each time step during the loading process, it is instructive to consider the continuous development of the cutting forces and the maximum temperature versus the increase in the cutting speed. This is illustrated in Fig. 11 for the cutting condition O3. For instance, the nonlinear increase in maximum temperature within Ω_{PSZ}, shown in Fig. 11 (right), is obtained without the need for simulations at multiple cutting speeds. In addition, a decrease in the feed force is observed with increasing cutting speed, while the cutting force initially decreases and then slowly increases. These trends are consistent through the subscale model.

Conclusion

In this study, a subscale model for material flow is developed in the primary and secondary shear zones to estimate the forces, stresses, and temperatures for the orthogonal cutting process. The model combines the coarse-grained kinematics of the DPZD model with the fine-grained subscale material flow governed by the NS equations. SUPG stabilization is included for all involved convection-dominated problems to gain control of possible oscillating solutions. In this context, a novel viscous/viscoplastic material flow model is developed on the JC constitutive model for orthogonal cutting simulation. In addition, a unique mixed method is developed for frictional contact of material flow to reduce spurious oscillations in contact stresses, typically associated with the conventional regularized frictional/contact formulation. The solutions to material flow and contact stresses are expressed explicitly, which contributes to a cost-effective solution procedure. It appears that when the DPZD approximation is included, the NS flow problem of the subscale velocity is more cost-effective (approx. 60% faster) than resolving the total velocity using the NS formulation of the problem. Compared to the DEFORM 2D simulations, the subscale model is also more robust and significantly less computationally demanding, since there is no requirement for remeshing. For the cases presented, it takes around 1.5 hours to run the subscale simulation, while this value is around 7 hours for the DEFORM 2D simulation. The trend of estimated forces and temperatures is consistent with the DEFORM 2D simulations and experimental data from the literature. However,

the feed forces are significantly underestimated compared to the measured values while the maximum temperature is approximately 100°C above the expected temperature range. Three different effects may be considered as the reason for the underestimation of feed forces: lack of tertiary shear zone, perfectly sharp tool assumption, and lack of plowing. The tertiary shear zone, and therefore the friction behavior in this contact region, would contribute to the increase in feed forces. Secondly, considering the rounded tool, an additional contact area would create forces in both the cutting and the feed directions. Finally, plowing causes the material to deform without cutting it because of the roundness of the tool edge, which affects the effective uncut chip thickness and the forces. In terms of temperature estimation, the model should be enhanced by including more realistic heat transfer from the system. Including these effects may increase the accuracy of the subscale model.

Funding Open access funding provided by Chalmers University of Technology. This study is funded by the Swedish Research Council (Project ID: 2021-05583).

Data Availability The datasets used or analyzed during this study are available from the corresponding author on reasonable request.

Declarations

Conflict of interest The authors declare that they have no conflict of interest.

References

1. Tay A, Stevenson M, Vahl Davis G (1974) Using the finite element method to determine temperature distributions in orthogonal machining. Proc Inst Mech Eng 188(1):627–638
2. Vaz M, Owen D, Kalhori V, Lundblad M, Lindgren L-E (2007) Modeling and simulation of machining processes. Arch Comput Methods Eng 14:173–204
3. Ambati R, Yuan H (2011) Fem mesh-dependence in cutting process simulations. Int J Adv Manu Technol 53:313–323
4. Seshadri R, Naveen I, Srinivasan S, Viswasubrahmanyam M, Vijay-Sekar KS, Pradeep Kumar M (2013) Finite element simulation of the orthogonal machining process with al 2024 t351 aerospace alloy. Procedia Eng 64:1454–1463
5. Strenkowski JS, Moon K-J (1990) Finite Element Prediction of Chip Geometry and Tool/Workpiece Temperature Distributions in Orthogonal Metal Cutting. J Eng Ind 112(4):313–318
6. Lin ZC, Lin SY (1992) A Coupled Finite Element Model of Thermo-Elastic-Plastic Large Deformation for Orthogonal Cutting. J Eng Mater Technol 114(2):218–226
7. Idelsohn SR, Oñate E, Del Pin F (2004) The particle finite element method: a powerful tool to solve incompressible flows with free-surfaces and breaking waves. Int J Numer Meth Eng 61:964–989
8. Rodríguez JM, Jonsén P, Svoboda A (2017) Simulation of metal cutting using the particle finite-element method and a physically based plasticity model. Comput Part Mech 4:35–51
9. Movahhedy M, Gadala MS, Altintas Y (2000) Simulation of the orthogonal metal cutting process using an arbitrary Lagrangian-Eulerian finite-element method. J Mater Process Technol 103(2):267–275
10. Arrazola PJ, A. Villar DU, Marya S (2007) Serrated chip prediction in finite element modeling of the chip formation process. Mach Sci Technol 11(3):367–390
11. Umbrello D (2008) Finite element simulation of conventional and high speed machining of ti6al4v alloy. J Mater Process Technol 196(1):79–87
12. Pantalé O, Bacaria J-L, Dalverny O, Rakotomalala R, Caperaa S (2004) 2d and 3d numerical models of metal cutting with damage effects. Comput Methods Appl Mech Eng 193(39):4383–4399
13. Rodriguez JM, Carbonell JM, Cante JC, Oliver J (2016) The particle finite element method (pfem) in thermo-mechanical problems. Int J Numer Meth Eng 107:733–785
14. Shi B, Attia H, Tounsi N (2010) Identification of Material Constitutive Laws for Machining-Part I: An Analytical Model Describing the Stress, Strain, Strain Rate, and Temperature Fields in the Primary Shear Zone in Orthogonal Metal Cutting. J Manuf Sci Eng 132(5):051008
15. Shi B, Attia H, Tounsi N (2010) Identification of Material Constitutive Laws for Machining-Part II: Generation of the Constitutive Data and Validation of the Constitutive Law. J Manuf Sci Eng 132(5):051009
16. Johnson GR, Cook W (1983) A constitutive model and data for metals subjected to large strains, high strain rates and high temperatures. In: Proc. 7th international symposium on ballistics, pp 541–547
17. Svenning E (2016) A weak penalty formulation remedying traction oscillations in interface elements. Comput Methods Appl Mech Eng 310:460–474
18. Tokpavi DL, Magnin A, Jay P (2008) Very slow flow of Bingham viscoplastic fluid around a circular cylinder. J Non-Newtonian Fluid Mech 154:65–76
19. Zisis T, Mitsoulis E (2002) Viscoplastic flow around a cylinder kept between parallel plates. J Non-Newtonian Fluid Mech 105:1–20
20. Leppert C, Dinkler D (2005) A fluid mechanical model for granular flow in silos. Proc Appl Math Mech 5
21. Jabir SM, Noorsyakirah A, Afian OM, Nurazilah MZ, Aswad MA, Afiq NHM, Mazlan M (2016) Analysis of the rheological behavior of copper metal injection molding (mim) feedstock. Procedia Chem 19:148–152
22. Kazban RV, Mason JJ (2007) Fluid mechanics approach to machining at high speeds: Part i: Justification of potential flow models. Mach Sci Technol 11(4):475–489
23. Kazban RV, Mason JJ (2007) Fluid mechanics approach to machining at high speeds: Part ii: A potential flow model. Mach Sci Technol 11(4):491–514
24. Klocke F, Brockmann M, Gierlings S, Veselovac D, Kever D, Roidl B, Schmidt G, Semmler U (2015) Analytical modelling methods for temperature fields in metal cutting based on panel method of fluid mechanics. Procedia CIRP 31:352–356

25. Gierlings S, Brockmann M (2013) Analytical modelling of temperature distribution using potential theory by reference to broaching of nickel-based alloys. In: WGP Congress 2013. Advanced Materials Research, vol 769, pp 139–146. Trans Tech Publications Ltd
26. Rokoš O, Ameen MM, Peerlings RHJ, Geers MGD (2020) Micromorphic computational homogenization for mechanical metamaterials with patterning fluctuation fields. J Mech Phys Solids 123:119–137
27. Donea J, Huerta A (2003) Finite Element Methods for Flow Problems. Wiley, Chichester, England
28. Grzesik W (2008) Advanced Machining Processes of Metallic Materials: Theory. Elsevier, Modelling and Applications
29. Erturk AS, Malakizadi A, Larsson R (2021) A thermomechanically motivated approach for identification of flow stress properties in metal cutting. Int J Adv Manuf Technol 111:1055–1068
30. Tobiska L, Lube G (1991) A modified streamline diffusion method for solving the stationary Navier-stokes equation. Numer Math 59:13–29
31. Malakizadi A, Cedergren S, Sadik I, Nyborg L (2016) Inverse identification of flow stress in metal cutting process using Response Surface Methodology. Simul Model Pract Theory 60:40–53
32. Abboud E, Shi B, Attia H, Thomson V, Mebrahtu Y (2013) Finite Element-based Modeling of Machining-induced Residual Stresses in Ti-6Al-4 V under Finish Turning Conditions. Procedia CIRP 8:63–68
33. Jafarian F, Imaz Ciaran M, Umbrello D, Arrazola PJ, Filice L, Amirabadi H (2014) Finite element simulation of machining Inconel 718 alloy including microstructure changes. Int J Mech Sci 88:110–121
34. Shi G, Deng X, Shet C (2002) A finite element study of the effect of friction in orthogonal metal cutting. Finite Elem Anal Des 38(9):863–883. https://doi.org/10.1016/S0168-874X(01)00110-X
35. Malakizadi A, Hosseinkhani K, Mariano E, Ng E, Del Prete A, Nyborg L (2017) Influence of friction models on FE simulation results of orthogonal cutting process. Int J Adv Manuf Technol 88(9–12):3217–3232
36. Yvonnet J, Umbrello D, Chinesta F, Micari F (2006) A simple inverse procedure to determine heat flux on the tool in orthogonal cutting. Int J Mach Tools Manuf 46(7):820–827
37. Huang S, Tao B, Li J, Fan Y, Yin Z (2018) Estimation of the time and space-dependent heat flux distribution at the tool-chip interface during turning using an inverse method and thin film thermocouples measurement. Int J Adv Manuf Technol 99:1531–1543
38. Buruaga M, Soler D, Aristimuño PX, Esnaola JA, Arrazola PJ (2018) Determining tool/chip temperatures from thermography measurements in metal cutting. Appl Therm Eng 145:305–314
39. Malakizadi A, Hosseinkhani K, Mariano E, Ng E, Prete A, Nyborg L (2016) Influence of friction models on FE simulation results of orthogonal cutting process. Int J Adv Manuf Technol 88:3217–3232